Journal of Mineralogical and Petrological Sciences, Volume 112, page 59–76, 2017

Serpentinite with and without brucite: A reaction pathway analysis of a natural serpentinite in the Josephine ophiolite, California

Yann Sonzogni[*], Allan H. Treiman[*] and Susanne P. Schwenzer[*,**]

[*]*Lunar and Planetary Institute, Houston, TX 77058–1113, United Sates of America*
[**]*The Open University, Department of Environment, Earth and Ecosystems, Walton Hall, Milton Keynes MK7 6AA, United Kingdom*

A partially serpentinized peridotite from the Josephine ophiolite has been studied in detail in order to characterize the chemical processes of its serpentinization. The original rock was harzburgite, and its olivine and orthopyroxene are partially replaced by veins and patches of lizardite serpentine and magnetite; brucite and talc are completely absent from the serpentinite, regardless of whether the precursor mineral was olivine or pyroxene. Petrographic and mineral–chemical data suggest at least two phases of serpentinization. Incipient serpentinization produced lizardite and magnetite veinlets, from preferential dissolution of orthopyroxene, and/or infiltration of a silica–rich fluid. No talc or brucite was produced, which suggests this serpentinization happened in a chemically open system. Later serpentinization was from a fluid closer to Fe–Mg–Si chemical equilibrium with the harzburgite, which should in theory favor formation of a brucite–bearing serpentinite. Brucite is absent from late serpentine veins, but they have some porosity which could represent former brucite that was dissolved out or was reacted out after serpentinization. Isocon modeling suggests that Si, Fe, and K were added during serpentinization and that Ca was lost; i.e., the serpentinization was not isochemical (except for H_2O). Results of petrographic observations, thermodynamic modeling, and mass balance calculations were used to constrain the reactions for global serpentinization of the studied sample. These reactions indicate that water with a concentration of H_2 up to two times that of deep sea vent fluids may have been produced during the serpentinization of the Josephine peridotite, which could then have been a potential host for significant biomass.

Keywords: Serpentine, Brucite, Dihydrogen, Peridotite–water reactions, Josephine ophiolite

INTRODUCTION

Serpentinization of ultramafic rocks is widespread near and along mid–ocean ridges, where mantle–derived peridotite is near the sea floor (e.g., Mével, 2003), and on land at convergent margins, where portions of oceanic lithosphere were obducted onto continental crust as ophiolites (e.g., Okland et al., 2012). Serpentinization of ultramafic rocks at spreading centers has significant effects on the geologic and geophysical properties of the oceanic lithosphere (e.g., Toft et al., 1990; Cannat et al., 1992; Cannat, 1993; Miller and Christensen, 1997; Escartín and Cannat, 1999; Gràcia et al., 2000; Escartín et al., 2001), as well as on chemical fluxes between seawater and exposed peridotites (e.g., Bach et al., 2004; Shervais et al., 2005). Serpentinization also produces H_2– and CH_4–rich fluids, which can support microbial communities in both seafloor and continental settings (e.g., Takai et al., 2004; Kelley et al., 2005; Blank et al., 2009). Such systems may be analogous to those of the early Earth where life originated, and to some environments where life might have existed and may persist today on other rocky planets (e.g., Schulte et al., 2006; Russell et al., 2010; Sleep et al., 2011). It is important, therefore, to characterize in detail peridotite–water reactions; however these are currently not well constrained in natural rock samples.

Based on petrographic, experimental, and theoretical investigations, two models have been proposed for the process of serpentinization. The first model is a two–stage process, involving early formation of brucite and serpentine (R1) followed by magnetite formation from the breakdown of primary brucite (R2) and serpen-

doi:10.2465/jmps.160509
Y. Sonzogni, sonzogni@lpi.usra.edu Corresponding author
A.H. Treiman, treiman@lpi.usra.edu
S.P. Schwenzer, susanne.schwenzer@open.ac.uk

tine (R3) (e.g., Toft et al., 1990; Oufi et al., 2002; Bach et al., 2006; Frost and Beard, 2007; Beard et al., 2009; Katayama et al., 2010; Frost et al., 2013). This process can be represented by the following idealized reactions:

$$\underset{\text{olivine}}{2(Mg,Fe)_2SiO_4} + \underset{\text{water}}{3H_2O} = \underset{\text{serpentine}}{(Mg,Fe)_3Si_2O_5(OH)_4} + \underset{\text{brucite}}{(Mg,Fe)(OH)_2} \quad \text{(R1)}$$

$$\underset{\text{brucite}}{9Fe(OH)_2} + \underset{\text{silica}}{4SiO_2} = \underset{\text{serpentine}}{2Fe_3Si_2O_5(OH)_4} + \underset{\text{magnetite}}{Fe_3O_4} + \underset{\text{water}}{4H_2O} + \underset{\text{hydrogen}}{H_2} \quad \text{(R2)}$$

$$\underset{\text{serpentine}}{Fe_3Si_2O_5(OH)_4} = \underset{\text{magnetite}}{Fe_3O_4} + \underset{\text{silica}}{2SiO_2} + \underset{\text{water}}{H_2O} + \underset{\text{hydrogen}}{H_2} \quad \text{(R3).}$$

The second model for serpentinization, on the other hand, involves a single step formation of serpentinite, brucite, and magnetite, as follows:

$$\underset{\text{olivine}}{8(Mg,Fe)_2SiO_4} + \underset{\text{water}}{10H_2O} = \underset{\text{serpentine}}{4(Mg,Fe)_3Si_2O_5(OH)_4} + \underset{\text{brucite}}{(Mg,Fe)(OH)_2} + \underset{\text{magnetite}}{Fe_3O_4} + \underset{\text{hydrogen}}{H_2} \quad \text{(R4).}$$

Both models require formation of brucite during serpentinization, but many serpentinized peridotites from both oceanic and continental settings lack brucite. The absence of brucite has been interpreted as representing either its complete reaction to serpentinite and magnetite upon continued fluid–rock interactions, or post-serpentinization weathering in which brucite was dissolved out (e.g., Bach et al., 2004, 2006; Beard et al., 2009; Frost et al., 2013).

Here, we studied a small volume of a partially serpentinized peridotite from the Josephine ophiolite, California, focusing on local mineral assemblages in order to characterize the chemical nature of its serpentinization reaction pathway. In particular, results indicate that brucite was absent from its early serpentinization products. Mineralogical and geochemical observations, and thermochemical calculations are used to constrain the serpentinization reaction pathway of the brucite-free peridotite, and gain a better understanding of the chemical fluxes that might apply on a larger scale. We emphasize that our primary purpose is not to unravel the serpentinization history of the whole Josephine Ophiolite, but to investigate small-scale serpentinization in great detail.

GEOLOGICAL SETTING AND SAMPLES

The Josephine ophiolite is located in the western Jurassic belt of the Klamath Mountains province, Southern Oregon and Northern California. It represents a complete ophiolite sequence overlain by silicic metasediments, the Galice Formation (Harper, 1984). The ophiolite has been dated at 157 ± 2 Ma and 164 ± 1 Ma (Saleeby et al., 1982; Wright and Wyld, 1986), and likely formed in a back-arc basin (e.g., Harper, 1980; Harper and Wright, 1984). The Josephine ophiolite and overlying Galice Formation were thrust eastward beneath the Klamath Mountains during the Nevadan orogeny, approximately 10 my after ophiolite formation.

This study focuses on a serpentinite from the Josephine peridotite body. The predominant lithologies in the Josephine peridotite body are harzburgite and dunite, with the latter representing <10% of its volume (Himmelberg and Loney, 1973; Loney and Himmelberg, 1976; Dick, 1977). The Josephine peridotite body experienced several episodes of serpentinization over a range of temperatures; high-temperature serpentinized shear zones developed when the peridotite body was close to the ridge-axis, while low-temperature serpentinization occurred during lateral transport of the oceanic lithosphere and during emplacement of the ophiolite (Harper, 1984; Norrell et al., 1989; Coulton et al., 1995). Approximately 70% of the peridotite body is partially serpentinized, and the extent of serpentinization is in many cases greater than 50% (Dick, 1974; Harper, 1984). The serpentinite for this study was collected in the Low Divide district, approximately 11 km east of Crescent City, California (Fig. 1). Rocks at Low Divide consist mainly of harzburgite and serpentinized harzburgite; massive ore formations consisting of Fe–Ni sulfide, native Fe–Ni metal, metal oxides, and Pt-bearing metal alloy are also present (Dunning and Cooper, 1995). Samples of serpentinites were collected at and away from the edge of a sulfide vein just to the north of Alta mine. The extent of serpentinization in our samples is inhomogeneous on the thin section scale, with almost completely serpentinized peridotites and relatively unserpentinized peridotites next to each other. For this study we selected a domain of net-veined serpentinite (~ 80% serpentinization) to investigate its alteration-reaction pathway.

METHODS

Analytical procedures

A standard petrographic thin section of the selected ser-

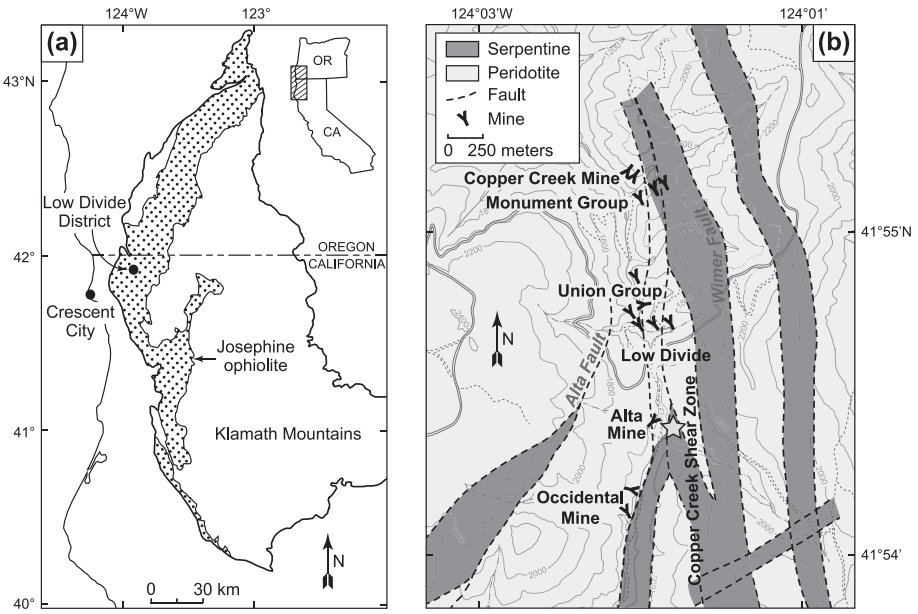

Figure 1. Field location. (a) Regional map of the Klamath Mountains province showing the Josephine ophiolite and the Low Divide district (modified from Irwin, 1972). (b) Geologic map of the Low Divide district area. The location of the sampling site is shown as a star (modified from Dunning and Cooper, 1995). Color version is available online from http://doi.org/10.2465/jmps.160509.

pentinite was examined by optical and scanning electron microscopy for mineralogy and alteration textures. Backscattered electron (BSE) and secondary electron (SE) images were acquired using the JEOL JSM6500 FEG-SEM at the ARES Division, Johnson Space Center. Mineral compositions were determined with the Cameca SX 100 electron microprobe at the ARES Division, Johnson Space Center, in wavelength dispersive mode. Natural silicates and oxides were used as calibration standards. A 15 kV accelerating voltage, 10 nA beam current on peak and on backgrounds, 30 seconds acquisition time, and 1 μm spot size were used for all analyses. Data were corrected using the Cameca ρ-φ-Z algorithm. Standard deviations (1σ) for oxides abundances are: <1% for oxides present at >10% weight; <5% for oxides present between 1 and 10% weight; <10% for oxides present between 0.1 and 1% weight; and <50% for oxides present at <0.1% weight. Raman spectra were collected for serpentine mineral identification using the Jobin-Yvon Horiba LabRAM HR800 Raman microprobe at the ARES Division, Johnson Space Center. A 514 nm Ar laser, 10 mW excitation power, and 20 seconds total acquisition time were used for all analyses. Calibration was performed before acquisition using a Si standard with a characteristic Raman peak at 520.4 cm^{-1}. The Raman spectrum from the glass slide and epoxy resin was acquired beforehand and then subtracted using the PeakFit®. Raman spectra were further processed in PeakFit® for best-fit baseline correction.

Geochemical modeling

We used thermochemical modeling to evaluate the conditions of formation of brucite-free serpentinization products from the original Low Divide harzburgite. For the geochemical models, we used CHIM-XPT (formerly CHILLER; Reed and Spycher, 2006; Reed et al., 2010), a code that was developed for and applied to terrestrial basaltic environments (e.g., Reed 1982, 1983). Computations of chemical equilibria are by a modified Newton-Raphson method. The code solves equations of chemical equilibria for aqueous species and minerals constrained by thermodynamic data, mass balance, mass action, and energy balance equations in its database; aqueous solutions are represented with an extended Debye-Hückel model (Reed 1982; Spycher and Reed, 1988; Reed 1998;). We have applied CHIM-XPT to a wide variety of post-magmatic, impact-generated and sedimentary alteration systems of mafic host rock compositions (e.g., Schwenzer and Kring, 2009; Bridges and Schwenzer, 2012; Schwenzer et al., 2012; Filiberto and Schwenzer, 2013; Schwenzer and Kring, 2013; Bridges et al., 2015; Melwani Daswani et al., 2016; Schwenzer et al., 2016;), including modelling towards the observed carbonate-phyllosilicate alteration succession in the nakhlite Martian meteorites (Bridges and Schwenzer, 2012).

The bulk composition of the original harzburgite (= unreacted host rock) was estimated from its modal mineral proportions and mineral compositions (Table 1). We estimated four possible bulk compositions for the harzburgite (harzburgites H1 to H4, Table 2), accounting for variations in pyroxene proportions observed in our samples and those reported in previous studies (Himmelberg and Loney, 1973; Dick, 1977; Harper, 1984). Cr-spinel has not been considered in the calculation of bulk compo-

Table 1. Average major element compositions for primary and alteration minerals in the Low Divide serpentinite

	Primary minerals					Alteration minerals				
	Ol (n = 31)	Opx (n = 4)	Cpx (n = 2)	Cpx_{Opx} (n = 1)	Chr (n = 1)	$SSrpo_{Ol}$ (n = 148)	$MSrpo_{Ol}$ (n = 89)	$SSrpo_{Opx}$ (n = 30)	$MSrpo_{Opx}$ (n = 38)	Mt (n = 7)
Oxides wt%										
SiO_2	40.55	57.49	52.59	53.15	0.05	42.37	42.40	42.72	42.39	0.77
TiO_2	0.01	0.02	0.03	0.02	0.08	0.01	0.01	0.01	0.02	0.01
Al_2O_3	0.02	1.18	2.26	2.71	16.82	0.24	0.18	0.10	0.89	0.00
Cr_2O_3	0.01	0.48	1.00	1.17	44.32	0.01	0.02	0.01	0.56	0.06
FeO_T [a]	9.16	5.92	2.57	2.42	24.83	3.18	4.02	2.84	3.92	91.01
MnO	0.14	0.16	0.09	0.08	0.31	0.05	0.07	0.07	0.15	0.19
NiO	0.38	0.11	0.05	0.08	0.03	0.32	0.35	0.36	0.19	0.04
MgO	49.10	33.99	18.34	17.31	8.64	40.41	39.50	40.04	37.84	0.15
CaO	0.04	1.30	22.34	21.78	0.00	0.06	0.05	0.02	0.04	0.00
Na_2O	0.00	0.01	0.11	0.02	0.00	0.02	0.02	0.03	0.02	0.00
K_2O	0.00	0.01	0.00	0.00	0.00	0.01	0.00	0.00	0.01	0.02
Total	99.43	100.68	99.39	98.73	95.08	86.68	86.62	86.20	86.04	92.25
Atoms (cation basis)										
Si	0.998	1.973	1.915	1.957	0.002	1.999	2.013	2.028	2.038	0.030
Ti	0.000	0.001	0.001	0.000	0.002	0.000	0.000	0.000	0.001	0.000
Al	0.001	0.048	0.097	0.118	0.669	0.013	0.010	0.006	0.051	0.000
Cr	0.000	0.013	0.029	0.034	1.183	0.000	0.001	0.000	0.021	0.002
Fe (II)	0.189	0.170	0.078	0.075	0.559	0.125	0.159	0.113	0.158	1.012
Fe (III) [b]					0.141					1.939
Mn	0.003	0.005	0.003	0.003	0.009	0.002	0.003	0.003	0.006	0.006
Ni	0.008	0.003	0.002	0.002	0.001	0.012	0.013	0.014	0.007	0.001
Mg	1.801	1.739	0.996	0.950	0.435	2.842	2.795	2.833	2.713	0.009
Ca	0.001	0.048	0.872	0.859	0.000	0.003	0.003	0.001	0.002	0.000
Na	0.000	0.001	0.008	0.001	0.000	0.002	0.002	0.002	0.002	0.000
K	0.000	0.000	0.000	0.000	0.000	0.000	0.000	0.000	0.001	0.001
Total cation	3.000	4.000	4.000	4.000	3.000	5.000	5.000	5.000	5.000	3.000
Molar composition										
Mg#	90.5	91.1	92.7	92.7		95.8	94.6	96.2	94.5	
En		88.9	51.2	50.4						
Fs		8.7	4.0	4.0						
Wo		2.5	44.8	45.6						

[a] FeO_T = Total iron as FeO.
[b] Calculated from stoichiometry.
Mg# = molar 100 MgO/(MgO + FeO). En, Fs, and Wo are the proportions of pyroxene end-members $MgSiO_3$, $FeSiO_3$, and $CaSiO_3$. Ol, Olivine; Opx, Orthopyroxene; Cpx, Clinopyroxene; Cpx_{Opx}, Clinopyroxene exsolution lamellae within orthopyroxene; Chr, Chromite; $SSrp_{Ol}$, Striated serpentine after olivine; $MSrp_{Ol}$, Massive serpentine after olivine; $SSrp_{Opx}$, Striated serpentine after orthopyroxene; $MSrp_{Opx}$, Massive serpentine after orthopyroxene; Mt, Magnetite; n, number of point analyses.

sitions, as it appears unaltered, with neither overgrowths (ferritchromite nor magnetite, as reported by Kimball, 1990; Burkhard, 1993) nor textures of dissolution.

The model calculations in CHIM-XPT were run to span a reasonable range of physical and chemical conditions for serpentinization of the Josephine peridotite. Modeled temperatures ranged from 200-350 °C, as described below in the text. Pressures ranged from 20-50 bars, high enough that the aqueous solution was only liquid (not gas) - reasonable variations in pressure have little effect on equilibrium positions in condensed systems like those we model here. Redox was controlled by initially setting all Fe to be FeO or Fe^{2+}(aq); there is minimal or no Fe^{3+} in the olivine or pyroxene of the Josephine peridotite, and we found minimal evidence for Fe^{3+} in any serpentine. Similarly, this peridotite contains no iron metal, although it is present in some areas of the Josephine peridotite. Our models were run at low salinity, $0.5*10^{-6}$ molar NaCl, which was just enough to allow CHIM-XPT to charge-balance the modelled solutions. We have no a priori way of knowing the salinity of the serpentinizing solutions, as the serpentine contains no Cl and no chloride minerals. Low to moderate salinity will affect our equilibrium models only by reducing the activ-

Table 2. Range of modal proportions and bulk chemical compositions for the original harzburgite and the serpentinite

	Original harzburgite				Serpentinite
	H1	H2	H3	H4	
Modal proportions (vol%)					
Ol	90.0	80.0	70.0	77.0	13.7
Opx	10.0	20.0	30.0	20.0	5.0
Cpx				3.0	
Srp					78.4
Mt					2.9
Chemical composition (wt%)					
SiO_2	42.37	43.96	45.56	44.33	40.83
TiO_2	0.01	0.01	0.01	0.01	0.01
Al_2O_3	0.13	0.24	0.36	0.31	0.33
Cr_2O_3	0.06	0.10	0.15	0.13	0.14
FeO	8.89	8.57	8.24	8.37	9.21
MnO	0.14	0.14	0.15	0.14	0.10
NiO	0.36	0.33	0.30	0.32	0.29
MgO	47.87	46.35	44.81	45.41	38.67
CaO	0.16	0.28	0.41	0.97	0.11
Na_2O	0.00	0.00	0.01	0.01	0.02
K_2O	0.00	0.00	0.00	0.00	0.01
Total	100.00	100.00	100.00	100.00	89.73

Ol, Olivine; Opx, Orthopyroxene; Cpx, Clinopyroxene; Srp, Serpentine; Mt, Magnetite. Modal proportions were weighted by mineral densities to give weight proportions. The densities (g/cm^3) were taken to be 3.38 for olivine, 3.27 for orthopyroxene, 3.40 for clinopyroxene, 2.59 for serpentine, and 5.15 for magnetite. Bulk chemical compositions were obtained by multiplying the weight proportion of each phase by the average composition of the phase. Average compositions for olivine, orthopyroxene, clinopyroxene, and magnetite are given in Table 1. Compositions of olivine, orthopyroxene, and clinopyroxene were normalized to 100% sum prior to calculations. Srp composition is the average of $SSrp_{Ol}$, $MSrp_{Ol}$, Srp_{Opx}, and $MSrp_{Opx}$ compositions (Table 1).

ity of H_2O in them, and that effect would not be apparent until unreasonably high salinities are reached. The system was modelled at water-to-rock ratios of 1:1 to 100000:1.

Many of the CHIM-XPT model results included small proportions of tephroite, Mn_2SiO_4, and grossular-andradite garnet, $Ca_3(Al,Fe^{3+})_2(SiO_4)_3$. These phases are not found in the natural alteration assemblages, and represent shortcomings of the chemical models and data inherent to CHIM-XPT (and similar programs). Tephroite appears as a separate phase because the models do not include Mn solid solution in olivine or serpentine – which is where the Mn resides in nature. Garnet appears in these (and other) models because the programs do not adequately represent Ca solid solution in olivine and solid solutions of Al and Fe^{3+} in pyroxene and serpentine. For completeness, we include these hypothetical phases in our descriptions of our model results, but caution the reader that their presence is a minor artifact of the modeling, and does not affect its utility for describing serpentinization.

RESULTS

Petrography

Whole rock. The target serpentinite consists of relics of primary olivine, orthopyroxene, clinopyroxene, and Cr-spinel surrounded by a network of cross-cutting veins of serpentine and magnetite (Fig. 2). Neither brucite nor other hydroxyl-bearing mineral (except serpentine) was identified by optical petrography, BSE/SE/Energy Dispersive Spectroscopy (EDS) imagery, Raman spectra, or electron microprobe (EMP) chemical analyses. The mineral proportions of the serpentinite, estimated from point counting on 10 BSE images covering the whole thin section (total surface ~ 5 cm^2, representing ~ 1000 olivine + pyroxene grains and ~ 90 million points), is 78 vol% serpentine, 14 vol% olivine, 5 vol% orthopyroxene, 3 vol% magnetite, and accessory clinopyroxene and Cr-spinel. Based on the proportions of remnant primary mineralogy, we interpret the protolith to be the common Josephine harzburgite, with original mineral proportions of 70–90 vol% olivine, 10–30 vol% orthopyroxene, 0–3 vol% clinopyroxene, and <2 vol% Cr-spinel (Himmelberg and Loney, 1973; Dick, 1977; Harper, 1984).

Olivine grains are 50–300 μm in size, mostly 100–200 μm, and roughly evenly distributed throughout the serpentinite (Fig. 2a). The initial size and shape of olivine crystals cannot be ascertained. Orthopyroxene occurs as large (up to 2 mm) grains that appear to retain their original crystal shape and thus seem to have been less affected by serpentinization (Fig. 2b). These large grains are, nonetheless, extensively fractured and crosscut by serpentine veins. Orthopyroxene crystals contain rare, narrow (<10 μm) exsolution lamellae of clinopyroxene. As a whole, the distribution of orthopyroxene is heterogeneous at the thin section scale. A single, almost unaltered clinopyroxene crystal ~ 300 μm in size was observed, adjacent to a large orthopyroxene. Cr-spinel occurs as subhedral grains <200 μm in size, mostly <50 μm, which appear unaltered.

Serpentine veins. Serpentine occurs almost entirely as veins between relics of primary minerals (Fig. 2); a few regions of massive, blocky serpentine are present. Veins vary in width from a few μm up to 500 μm, most being ~ 100 μm. They are oriented in all directions, although the larger veins (>100 μm across) show a preferred orientation. Relic grains along these subparallel serpentine veins are elongated along the long axis of the veins, and so likely their precursors. Bach et al. (2006), Beard et al. (2009), and Frost et al. (2013) recognized two types of veins in serpentinized peridotites from the Mid-Atlantic ridge and the New Caledonian ophiolite; narrow intragranular veins consisting of serpentine and

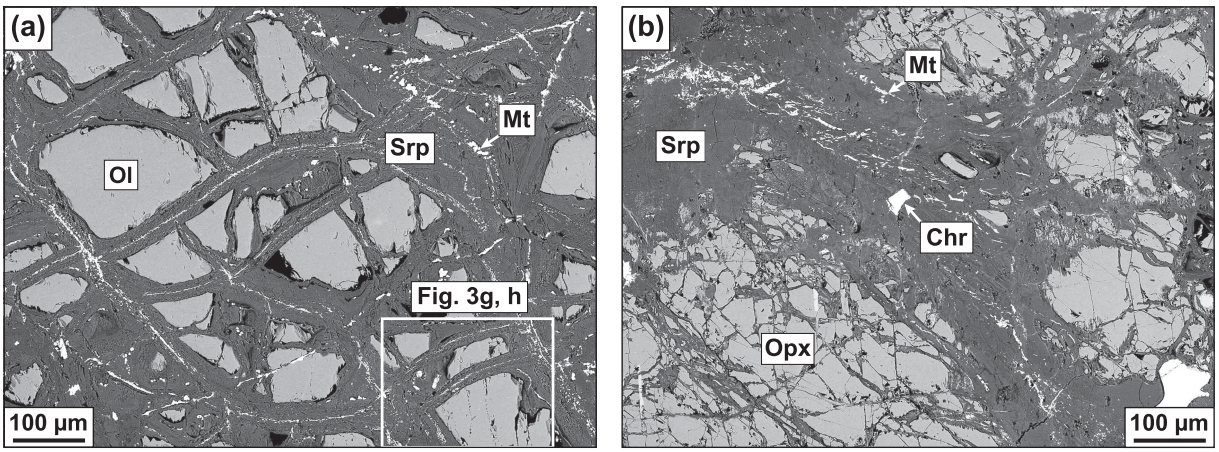

Figure 2. Back-scattered electron images showing the typical textures of partially serpentinized peridotite from the Josephine ophiolite at Low Divide. All veins contain both serpentine and magnetite, independent with their size and the nature of the surrounding mineral. See Figure 3 for images of individual veins. (a) Serpentine and magnetite veins surrounding olivine (Ol) relics. Narrow (<100 µm) veins in the center and center-left regions likely correspond to intragranular veins across a former olivine crystal; the wider (~ 200 µm) vein running from the top-center to the bottom-right corner of the image probably is an intergranular vein. Box shows the location of images in Figure 3g and h. (b) Wide (~ 200 µm) and narrow (<50 µm) serpentine and magnetite veins across a large (~ 1.5 mm) orthopyroxene (Opx) crystal. Two chromites (Chr) grains (brightest) are visible.

brucite, and wider intergranular veins consisting of serpentine, magnetite, and accessory brucite. In the serpentinite studied here, the distinction between intergranular and intragranular veins is difficult for veins surrounding olivine, because olivine grains have similar size and are evenly distributed. However, regardless of local setting, all of the serpentine veins are similar, and consist of >90% serpentine and <10% magnetite (Fig. 3). There are no mineralogical differences between narrow and large veins, nor between veins surrounding olivine relics and those surrounding pyroxene relics.

The serpentine in the veins can be divided into two textural varieties, based on BSE imaging: striated, and massive (Fig. 3). This difference is also apparent in SE and reflected-light optical images of polished surfaces; striated serpentine (henceforth referred as SSrp) is less resistant to polishing than the massive serpentine (henceforth referred as MSrp), and thus its polished surfaces are at lower 'elevation' than the surrounding olivine. High magnification, FEG-SEM images show that the striated texture of the SSrp is due to darker lineations, <1 µm wide and <10 µm long, that represent void spaces (i.e., porosity) (Fig. 4). In addition, SSrp veins usually consist of multiple internal bands of serpentinite; the bands themselves are parallel with the overall vein orientation but the orientation of void spaces differs from one band to the next. In some case, bands of SSrp with void spaces having a given orientation are distributed symmetrically around the center of the vein.

For several reasons, the void spaces in the serpentine veinlets cannot be merely artifacts of sample preparation. First, the serpentinite samples were impregnated with epoxy and polished carefully. Second, serpentine veins of different orientation contain both SSrp and MSrp, which would not be so a likely result of sample preparation. And third, the presence of void spaces in the SSrp distributed symmetrically across the vein centers suggests that void spaces are inherent to the SSrp. The proportion of void spaces in a vein, estimated from point counting on BSE images from 10 SSrp veins, is <7 vol%.

Narrow (<50 µm) serpentine veins contain either SSrp or MSrp (Figs. 3a, 3b, 3d, 3e); larger veins usually contain both types (Figs. 3c and 3f). No correlation was observed between the texture of the serpentine and the nature of the precursor mineral. Although cross-cutting relationships between SSrp veins and MSrp veins are in most cases ambiguous, there is textural evidence that the SSrp is more recent than the MSrp. An example is given in Figure 3g, h, where veins of SSrp cut across, and are in contact with both MSrp and olivine. One could argue that the MSrp in this area replaced olivine after the SSrp had formed. However, this does not fit with the observation that MSrp is present as a thick mantle on two edges of the olivine crystals (right and left edges on Figs. 3g and 3h), and absent on the other two edges (top and bottom edges on Figs. 3g and 3h). Thus, we interpret these cross-cutting relationships as evidence that the SSrp post-dates the MSrp.

Magnetite is present in all of the veins, regardless of the texture (SSrp or MSrp or both) and the size of the veins (Fig. 3). In most veins, magnetite occurs as a single or multiple massive bands near the center or on the edge of the veins, and as isolated grains elsewhere; in other veins,

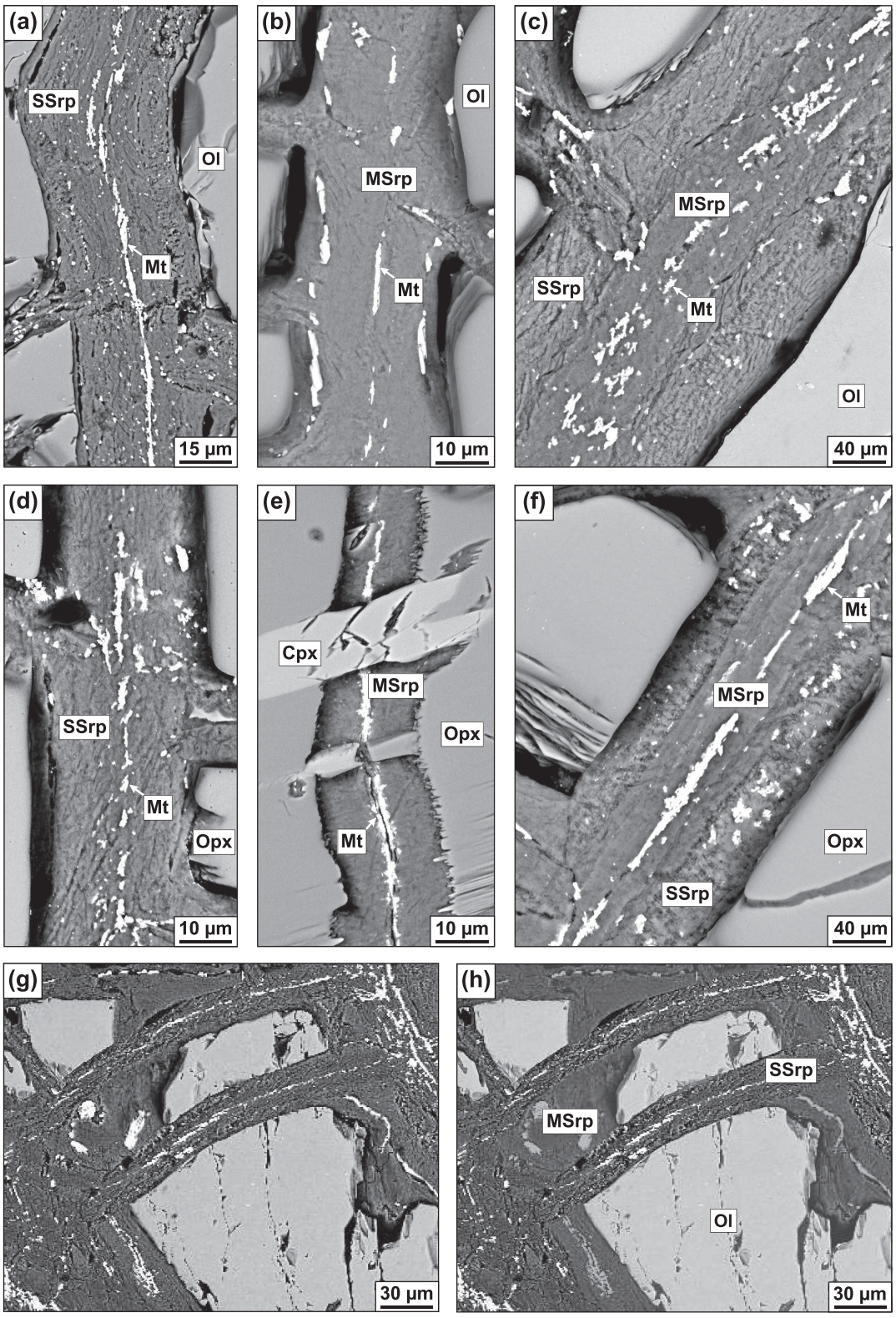

Figure 3. Back-scattered electron images showing the characteristic textures of serpentine-magnetite veins. (a) Narrow vein of striated serpentine (SSrp) and magnetite (Mt) cutting olivine (Ol). (b) Narrow veins of massive serpentine (MSrp) and magnetite cutting olivine. (c) Large vein of massive and striated serpentine and magnetite cutting olivine. (d) Narrow vein of striated serpentine and magnetite cutting orthopyroxene (Opx). (e) Narrow vein of massive serpentine and magnetite cutting orthopyroxene. (f) Large vein of massive and striated serpentine and magnetite cutting orthopyroxene. (g), (h) Late striated serpentine (SSrp) cutting through early massive serpentine (MSrp) and olivine. Color version is available online from http://doi.org/10.2465/jmps.160509.

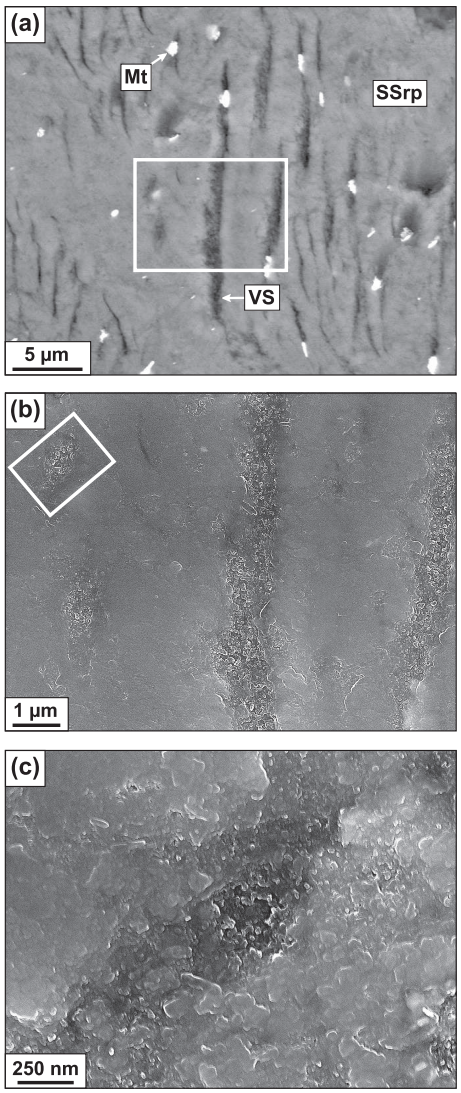

Figure 4. Back-scattered (a) and secondary electron (b), (c) images illustrating the void spaces in the striated serpentine. Box in (a) shows the location of image (b); box in (b) shows the location of image (c). SSrp, Striated serpentine; Mt, Magnetite; VS, Void space.

magnetite is present as sparse grains only. Massive magnetite occurs as either a continuous band of µm-sized magnetite grains or a trail of isolated, coarser (<20 µm) grains. The width of magnetite bands and trails, ranging from a few µm up to 50 µm, increases with vein width (although continuous magnetite bands rarely exceed 10 µm in thickness). Magnetite grains outside massive bands are <5 µm.

Raman spectroscopy

To determine which serpentine polymorph was present, we collected Raman spectra across fourteen SSrp and MSrp veins around olivine and orthopyroxene grains. For each vein, we acquired spectra from one edge of the vein to the other. All the Raman spectra are consistent with lizardite serpentine, and not with chrysotile or antigorite (Fig. 5). This identification is consistent with the planar and flaky texture of the serpentine mineral, which is also characteristic of lizardite (Fig. 6). By extension, the observation that serpentine has a foliate texture in all of the other veins (~ 25) investigated at high magnification suggests that lizardite is the dominant serpentine polymorph present in the serpentinite. Noteworthy, the position, shape, and intensity of Raman peaks across an individual vein are insensitive to the texture of the serpentine (SSrp or MSrp, Fig. 5). This indicates that the difference in serpentine texture is unlikely to be due to different crystallographic orientations of the serpentine mineral, as also suggested by high magnification imaging.

None of the Raman spectra showed any scattering peaks consistent with brucite or talc or any other minerals besides olivine, pyroxene, and magnetite. These non-detections are consistent with the non-detections by optical microscopy and EMP chemical analyses.

Mineral chemistry

To determine primary minerals compositions and investigate the chemistry of the serpentine mineral across individual veins, we obtained electron microprobe chemical analyses on linear traverses across 21 veinlets, 17 of which were bordered by olivine and 4 of which were bordered by orthopyroxene. Table 1 reports the average major element compositions for primary and alteration minerals, and Figure 7 illustrates the Fe-Mg-Si distribution of analysis spots for the whole dataset.

Precursor minerals. The compositions of the primary silicate and oxide minerals are typical of those in mantle peridotite (Table 1). Olivine is chemically unzoned and homogeneous in composition, Fo_{90-91}, with MnO = 0.11-0.18 wt%, and NiO = 0.32-0.42 wt%. Orthopyroxene has a Mg# of 91, and contains 0.94-1.54 wt% CaO, ~ 1.2 wt% Al_2O_3, and ~ 0.5 wt% Cr_2O_3. The larger clinopyroxene grain is diopside, $En_{51}Fs_4Wo_{45}$, with 2.3 wt% Al_2O_3, and 1.0 wt% Cr_2O_3. Clinopyroxene lamellae in orthopyroxene are also diopside, $En_{50}Fs_4Wo_{46}$, with 2.7 wt% Al_2O_3, and 1.2 wt% Cr_2O_3. The spinel phase is chromite: $Chr_{59}Sp_{34}Mt_{07}Usp_{00}$ (Chr, Chromite; Sp, Spinel; Mt, Magnetite; Usp, Ulvöspinel). These mineral compositions are consistent with those reported in previous studies of the Josephine harzburgite (Dick, 1977; Harper, 1984).

Serpentine. Most (~ 95%) of microprobe analyses across the veins plot close to the Mg-serpentine (lizardite) endmember in Figure 7, consistent with Raman spectroscopy measurements. A few analyses lie along a mixing line between serpentine and magnetite, suggesting that they

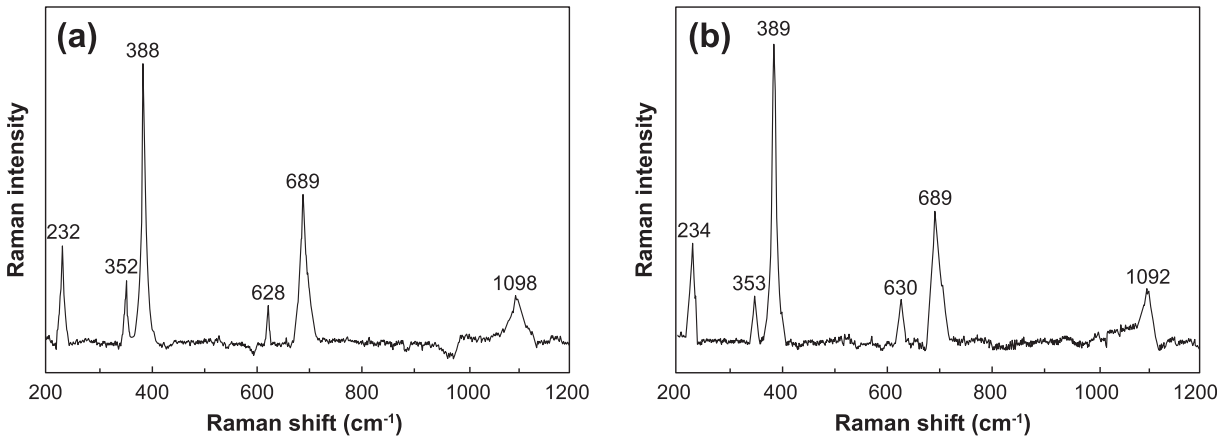

Figure 5. Characteristic Raman spectra of striated serpentine veinlets (a) and massive serpentine veinlets (b). Spectra were acquired in the same veinlet. Labeled peaks are typical of lizardite. Typical peaks of chrysotile (345 cm^{-1}, 620 cm^{-1}, 1105 cm^{-1}), antigorite (375 cm^{-1}, 520 cm^{-1}, 1044 cm^{-1}), and brucite (280 cm^{-1}, 443 cm^{-1}) are absent. Reference spectra for serpentine minerals are from Rinaudo et al. (2003) and Groppo et al. (2006), and for brucite from Dawson et al. (1973).

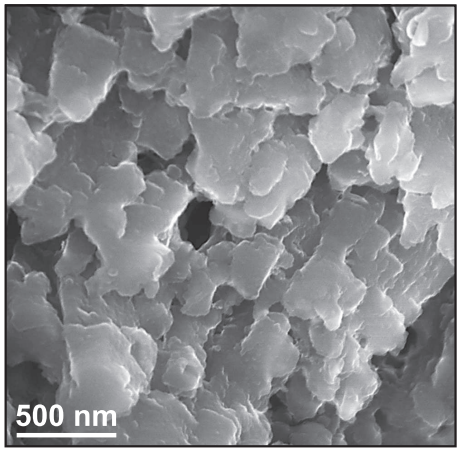

Figure 6. Secondary electron image illustrating the flaky texture of the serpentine mineral, typical of the lizardite polymorph.

represent analytical volumes that contain lizardite and magnetite. A few analyses fall near a line between the lizardite compositions and that of the ferric iron serpentines Fe-cronstedtite and Mg-cronstedtite. These rare analyses are all near massive magnetite bands in the veins, and are not significant in terms of bulk composition of the serpentine veinlets or in mass balance calculations. There is no indication that any Fe^{3+}-serpentine or greenalite are present. Microprobe analyses give no indications of brucite and talc in the veins, as shown both by the absence of EMP analyses on serpentine-brucite and serpentine-talc mixing lines in Figure 7, and by the nearly stoichiometric composition of the serpentine minerals (Table 1).

The average compositions of serpentines vary only slightly depending on texture (SSrp or MSrp) and the precursor mineral (olivine or orthopyroxene), see Table 1. Serpentine between olivine grains averages 42.5 wt% SiO_2, 39.5–40.5 wt% MgO, and 3–4 wt% FeO, and has a Mg# of 95–96; serpentine crossing orthopyroxene grains averages 42.5 wt% SiO_2, 38–40 wt% MgO, and 3–4 wt% FeO, and has a Mg# of 94–96. Concentrations of other cations (e.g., Ni, Cr, Al, and Ca) also vary little among and between types of serpentine. However, massive serpentine between orthopyroxene grains generally contains more aluminum (0.9 wt% Al_2O_3) and chromium (0.6 wt% Cr_2O_3) than its striated counterpart and serpentine between olivine grains.

DISCUSSION

Evaluating the possibility of secondary brucite loss

The serpentinite studied here lacks both brucite and talc; neither mineral was detectable by optical petrography, BSE/SE/EDS imagery (Fig. 3), Raman spectroscopy (Fig. 5), or electron microprobe point analyses (Fig. 7). Brucite can be abundant in alpine serpentinites (e.g., Hostetler et al., 1966), but the absence of brucite and talc is common in serpentinized harzburgites and dunites. In fact, brucite has been reported to be rare or absent in serpentinites from both oceanic and continental settings (e.g., Miyashiro et al., 1969; Page, 1976; Aumento and Loubat, 1971; Ramana et al., 1981; Auzende et al., 2002; Andreani et al., 2004; Shervais et al., 2005; Andreani et al., 2007; Da Costa et al., 2008; Nakamura et al., 2009; Lafay et al., 2013). Similarly, talc is commonly absent from serpentinites of all varieties (e.g., Coleman and Keith, 1971; Page, 1976; Shervais et al., 2005; Bach et al., 2006; Andreani et al., 2007; Lafay et al., 2013).

Brucite is not present in the Low Divide serpentinite, two possible explanations arise:

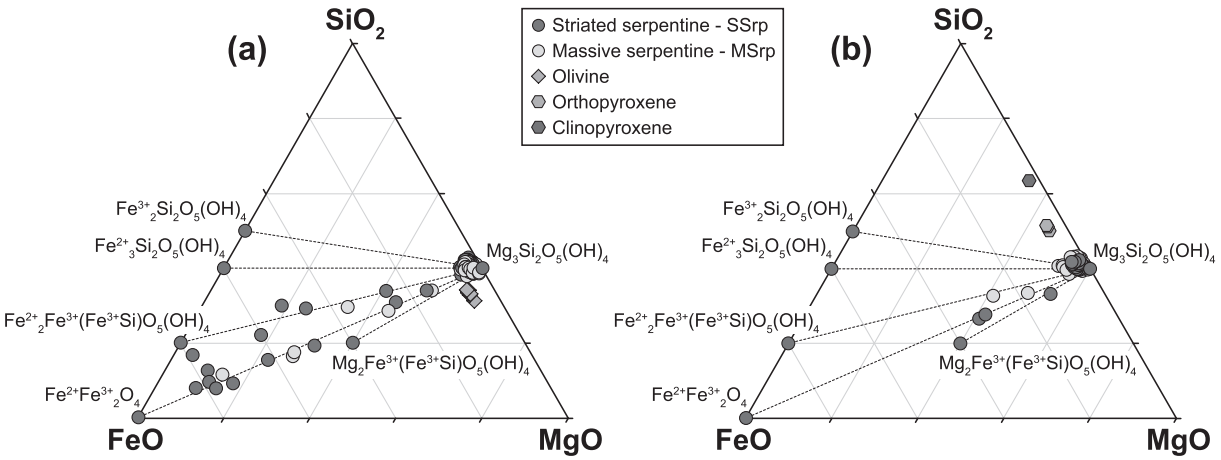

Figure 7. FeO–MgO–SiO_2 (molar proportions) ternary plots of serpentine mineral compositions from veins between olivine grains (a) and orthopyroxene grains (b). Serpentine Mg–Fe^{2+}–Fe^{3+} solid-solutions (dotted lines) and end-members (grey circles) are also indicated. Serpentine end-members are Mg-serpentine $Mg_3Si_2O_5(OH)_4$, greenalite $(Fe^{2+},Fe^{3+})_{2\text{-}3}Si_2O_5(OH)_4$, cronstedtite $Fe^{2+}{}_2Fe^{3+}(Fe^{3+}Si)O_5(OH)_4$, and Mg-cronstedtite $Mg_2Fe^{3+}(Fe^{3+}Si)O_5(OH)_4$. Magnetite $Fe^{2+}Fe^{3+}{}_2O_4$ is also shown. Serpentine data include 148 point analyses from 11 veins for striated serpentine after olivine, 89 point analyses from 10 veins for massive serpentine after olivine, 30 point analyses from 2 veins for striated serpentine after orthopyroxene, and 38 point analyses from 3 veins for massive serpentine after orthopyroxene. See text for explanations. Color version is available online from http://doi.org/10.2465/jmps.160509.

First, void spaces in the SSrp veins could represent an original feature of the serpentinization, or they could have developed afterwards by dissolution of brucite. Numerous experimental studies showed that brucite is highly soluble and rapidly dissolves in cold seawater (e.g., Lin and Clemency, 1981; Jordan and Rammensee, 1996; Pokrovsky and Schott, 2004), and the absence of brucite in natural serpentinites is commonly interpreted as post-serpentinization weathering in which brucite was dissolved out (e.g., Snow and Dick 1995). The proportion of void spaces in the SSrp provides a test of this hypothesis. In most serpentinites, brucite typically is intergrown with serpentine (e.g., Beard et al., 2009; Okland et al., 2012), consistent with the idealized reactions for isochemical serpentinization of olivine (R1) (Bach et al., 2006; Beard et al., 2009; Frost et al., 2013) and (R4). Bach et al. (2006), Beard et al. (2009), and Frost et al. (2013) proposed that serpentinization is a two-stage process in which brucite forms from olivine and then later reacts to serpentine and magnetite. This model is based on the observation that in serpentinites from oceanic settings, narrow early serpentine veins contain brucite and no magnetite, and larger later serpentine veins contain magnetite in the core and brucite on the margins. However, SSrp veins in the Low Divide serpentinite have the same mineralogy regardless of their size, i.e., serpentine + magnetite, and magnetite occurs both in the core and on the margins of the veins (Fig. 3). This does not support a step-like process, but suggests instead a single serpentinization reaction similar to reaction (R4). For the SSrp, one can write a more realistic reaction for isochemical serpentinization, from an initial harzburgite of 70 vol% olivine and 30 vol% orthopyroxene of the appropriate compositions:

$$\underset{826\ cm^3}{19.00(Mg_{0.9}Fe_{0.1})_2SiO_4} + \underset{348\ cm^3}{11.00(Mg_{0.91}Fe_{0.09})SiO_3} + 32.31H_2O = \underset{1631\ cm^3}{15.00(Mg_{0.95}Fe_{0.05})_3Si_2O_5(OH)_4} + \underset{36\ cm^3}{1.46Mg(OH)_2} + \underset{38\ cm^3}{0.85Fe_3O_4} + 0.85H_2 \quad \text{(R5)}.$$

Serpentinite formed by reaction (R5) should contain 96 vol% serpentine, 2 vol% brucite, and 2 vol% magnetite; if this reaction occurred in the Low Divide serpentinite and brucite had been dissolved away, one should expect the resultant serpentinite to contain ~ 2 vol% void spaces. The SSrp veins exhibit <7 vol% void spaces, which is consistent with dissolution of brucite from a serpentinite formed by reaction (R5). Reaction (R5) produces pure-Mg brucite, which may not be realistic. In the extreme case where all Fe from primary minerals that is not incorporated in serpentine is allotted to brucite, reaction (R5) produces 4 moles of brucite with composition $(Mg_{0.36}Fe_{0.64})(OH)_2$, equivalent to ~ 7 vol% brucite in the serpentinite. Again, this is consistent with the formation of void spaces in the SSrp by dissolution of brucite from a serpentinite formed by reaction (R5).

Magnesium released in solution by brucite dissolution might be involved in carbonate precipitation. In the nearby Coast Range ophiolite, meteoritic waters circulating through its peridotites react and yield highly alkaline Ca-OH and Mg-OH spring waters (e.g., Barnes et al.,

1967; Barnes and O'Neil, 1969; Barnes et al., 1972; Blank et al., 2009). Mg–Ca carbonate cements are commonly associated with these springs, which are presumably the sources of cations in the carbonate cements. Veins consisting of serpentine + dolomite occur in serpentinites of the Josephine ophiolite (Coulton et al., 1995), and carbonate deposits have been identified along fractures in rocks from Low Divide (Dunning and Cooper, 1995). It is possible that the magnesium released by brucite dissolution be the precursor of these deposits.

And, second, void spaces in the SSrp veins may result from volume expansion of peridotite during serpentinization. Serpentinization of the Josephine peridotite produced a kernel pattern of serpentine veins and relic olivine and pyroxene that is characteristic of volume expansion (O'Hanley, 1992). Estimates of volume increase for serpentinites from continental settings range from 25 to 60% (e.g., Coleman, 1971; O'Hanley and Offler, 1992; Shervais et al., 2005). Thus, all the porosity in the SSrp veins could be explained by volume expansion. Because brucite is absent from the SSrp veins, it is not possible to tell whether void spaces in these veins represent original porosity formed during serpentinization, or whether they represent dissolution of brucite after serpentinization. It would be very helpful to understand the textures of brucite-bearing serpentinites, at the scale we examined here (e.g., Andreani et al., 2004).

Serpentinization without brucite

The MSrp veins have essentially zero porosity, suggesting that they could not represent serpentinization by reaction (R1), (R4), or (R5), followed by dissolution of brucite. The two-step serpentinization model of Bach et al. (2006), Beard et al. (2009), and Frost et al. (2013) is not relevant for the MSrp veins either, because they do not contain brucite and do contain magnetite, regardless of their size. Petrographic and chemical data suggest rather that brucite was never present in the MSrp veins, and that magnetite was an initial product of serpentinization.

Reaction pathways can be tested further using thermochemical calculations (see section 3.2 for methodological details). Reacting any of the calculated original bulk rock compositions (Table 2) under the conditions described in section 3.2 produces brucite in the alteration mineralogy. The lowest brucite content is produced using the most orthopyroxene-rich harzburgite (H3, Table 2). Hydration of the H3 composition results in an alteration assemblage consisting of approximately 91 vol% serpentine, 3.9 vol% magnetite, 2.9 vol% brucite, and 2.2 vol% of chlorite (plus small proportions of garnet and tephroite), see Figure 8a. This result is consistent with

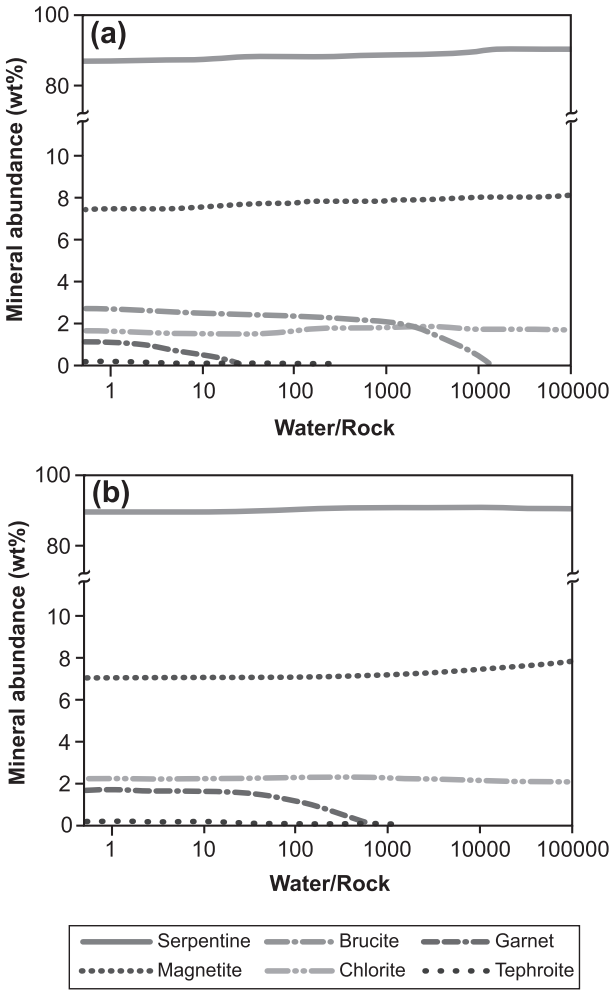

Figure 8. Alteration mineralogy predicted by CHIM-XPT models over a range of water-to-rock ratios for (a) harzburgite composition H3 (Table 2) reacted with water at 200 °C and 20 bars and (b) harzburgite composition H3 with 10 vol% added orthopyroxene (Table 1) reacted with water at 200 °C and 20 bars. Water to rock ratio in the model is defined as mass ratio of rock dissolved in a given amount (1 kg) of fluid. See text for discussion of the results. Color version is available online from http://doi.org/10.2465/jmps.160509.

previous studies by Bach et al. (2006), Beard et al. (2009), and Frost et al. (2013), which concluded that orthopyroxene hydration during serpentinization of harzburgite produced high silica activity in the fluid which stabilizes the assemblage serpentine + magnetite rather than brucite (reaction (R2)).

Brucite is absent from the alteration mineralogy when the system is richer in Si and poorer in Mg than the harzburgite composition H3. To achieve such a system, we assumed incongruent dissolution of the harzburgite with preferential dissolution of orthopyroxene. Experimental reactions of peridotite with seawater and seawater-derived solutions at 200–300 °C, 350–500 bars,

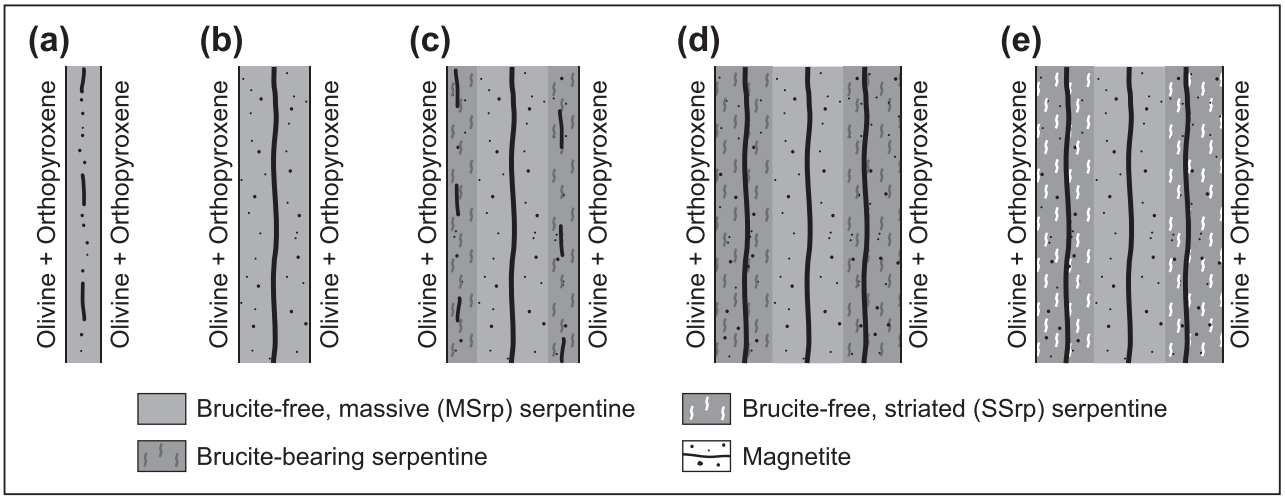

Figure 9. Formation of serpentine veins. (a) Growth of brucite-free, massive (MSrp) serpentine. Magnetite growth initiates in the center of the vein. (b) Continued growth of massive serpentine. Magnetite preferentially grows on pre-existing grains in the vein center, forming a massive magnetite band, and grows as isolated grains elsewhere. (c) Growth of brucite-bearing serpentine and magnetite. (d) Development of multiple magnetite bands as vein growth continues. (e) Post-serpentinization dissolution of brucite, leaving void spaces in late serpentine veins and forming the striated (SSrp) serpentine. Color version is available online from http://doi.org/10.2465/jmps.160509.

and 10-30 water-to-rock ratios showed that enstatite and olivine dissolution rates are similar over the course of the experiments, but that enstatite reacts out faster than olivine during the initial steps of serpentinization due to its higher chemical affinity in the initial seawater composition (Janecky and Seyfried, 1986; Klein et al., 2015). These experiments also showed that preferential dissolution of orthopyroxene gives brucite-free alteration assemblages. To model preferential hydration of orthopyroxene, we used a starting harzburgite of the H3 composition with 10 vol% added orthopyroxene (i.e., 65 vol% olivine + 35 vol% orthopyroxene). Modeling reaction of this mixture with water at 200 °C and 20 bars (i.e., in conditions appropriate for the presence of lizardite, see section 4.2) results in a brucite-free mineral assemblage of approximately 93 vol% serpentine, 3.6 vol% magnetite, and 3.4 vol% chlorite (plus small proportions of garnet and tephroite), see Figure 8b. An alternative scenario equally explaining the production of a brucite-free assemblage is addition of a fluid bringing ~ 1 mole Si/kg dissolving harzburgite to the harzburgite composition H3. Chlorite, garnet, and tephroite are minor phases in the models. Chlorite is present at a maximum of 2.45 wt%. If we assume that the serpentine was mixed-layer chlorite-serpentine, up to 2.6 wt% of the serpentine would be mixed layered serpentine, which we consider below the detection limit of the electron microprobe analysis. We also point out that we observed no peak shift or broadening in Raman spectra of the serpentine that would indicate the presence of any of the minor phases in the models. Therefore, the above models successfully reproduce the phase proportions in the MSrp veins (i.e., >90% serpentine, <10% magnetite).

An important result arising from the absence of brucite in the MSrp veins is that the initial serpentinization at Low Divide must have acted in an open chemical system. This inference is at odds with some earlier models. In their two-step serpentinization model, Bach et al. (2006), Beard et al. (2009), and Frost et al. (2013) suggested that the transition from brucite-bearing veins to brucite-free veins reflects a transition from isochemical, rock-dominated serpentinization to an open-system, fluid-dominated serpentinization. The authors argued that open-system serpentinization allows access of silica (mostly produced by hydration of orthopyroxene), causing brucite to react to serpentine + magnetite [reaction (R2)]. Here, the lack of brucite in the smallest MSrp veins suggest that the fluid flow regime was active enough so that orthopyroxene and olivine were in chemical communication during the initial stages of MSrp vein formation, and silica produced by serpentinization of orthopyroxene was consumed by the olivine hydration reaction to form serpentine and magnetite; this precluded the formation of high-silica (i.e., talc-bearing) domains around orthopyroxene and low-silica (i.e., brucite-bearing) domains around olivine. Because MSrp veins pre-date SSrp veins, this suggests that the system was open at the inception of serpentinization.

Serpentinization history

Petrographic and chemical data, as well as thermodynamic modeling provide us with a model for the serpentinization history at Low Divide (Fig. 9). Harzburgite of H3

composition (Table 2) was infiltrated by a fluid at ~ 200 °C. During the initial steps of serpentinization, orthopyroxene dissolved faster than olivine. Open-system conditions prevented gradients in silica activity to build up between orthopyroxene and olivine, so that talc and brucite precipitation was inhibited, and serpentine and magnetite formed as initial products of serpentinization. This initial event formed the massive serpentine. An alternative scenario to form the massive serpentine is that the fluid that infiltrated the H3 harzburgite was equilibrated at high temperature before cooling to ~ 200 °C at the serpentinization site. Cooling decreased the solubility of silica in the fluid, and thus added silica to the system. Such system allowed congruent dissolution of olivine and orthopyroxene under open-system, high silica activity conditions to form serpentine and magnetite.

A second phase of serpentinization can be inferred to involve a fluid that was closer to equilibrium with the harzburgite; dissolution of orthopyroxene would not have been favored over dissolution of olivine. This second phase formed the striated serpentine (originally containing brucite) and associated magnetite. Brucite is not now observed in the striated serpentine veins; we infer that the porosity of those veins represents, at least in part, brucite that dissolved out during later stages of alteration.

Mass transfer

To estimate mass transfer associated with serpentinization, we used the isocon diagram method of Grant (1986, 2005), see Figure 10, which has been extensively used to investigate serpentinization (e.g., Shervais et al., 2005; Augustin et al., 2008; Jöns et al., 2010; Evans et al., 2013; Frost et al., 2013). The isocon diagram compares the composition of the altered rock to that of the original rock. In the idealized isocon diagram, element abundances that are not modified during serpentinization should all lie on a single line (the isocon) that runs to the origin (Fig. 10). Oxides that have been added to the system should lie above that line, and oxides that have been extracted should lie below the line. The slope of the isocon line depends on the mass and volume change of the rock during alteration. In the real world, the location of an isocon line for a metasomatic process must be estimated because: the composition of the original rock cannot be known (it is no longer present), the analyzed composition of the altered rock may not be representative of the whole rock body (especially in minor elements like Ti), and the chemical analyses may not be precise (especially for minor elements).

Our best-estimate isocon line for our serpentinite sample is shown in Figure 10, and is based entirely on the rocks of the Low Divide area, and not on an assumption of constant mass or of constant volume. We used harzburgite H3 (Table 2) as the composition of the original rock (see section 5.2), and the bulk composition of the present serpentinite was calculated from its mineral proportions and mineral compositions (Tables 1 and 2). Because the composition of serpentine varies only slightly depending on its texture (SSrp or MSrp) and the nature of the precursor mineral (olivine or orthopyroxene), our calculation used the average composition of all serpentine types. On Figure 10, points representing several elements that are reasonably immobile in serpentinizing fluid are co-linear with each other and with the origin: TiO_2, Al_2O_3, and Cr_2O_3. These element abundances (and the origin) define an estimated isocon for Low Divide; within the uncertainties of rock and chemical analyses, it seems reasonable that MgO, MnO, and Na_2O were also immobile during serpentinization (i.e., they fall near or on the estimated isocon).

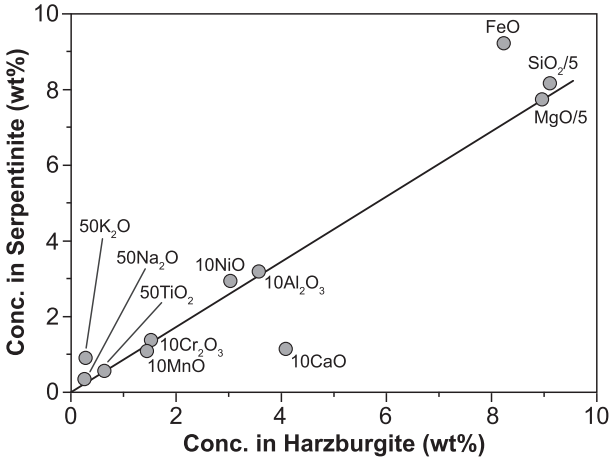

Figure 10. Isocon diagram for the original harzburgite and the serpentinite at Low Divide. A best-fit isocon is estimated, with a slope of 0.90, corresponding to a mass increase of 10 percent and a volume increase of 30 percent (assuming densities (g/cm^3) of 3.35 for the harzburgite and 2.8 for the serpentinite). See text for discussion.

However, serpentinization of the Josephine peridotite at Low Divide was not isochemical (Fig. 10). The estimated best-fit isocon suggests that serpentinization increased the original rock's abundances of SiO_2 by ~ 2%, NiO by ~ 7%, FeO by ~ 25%, and K_2O by ~ 60%. These additions were accompanied by a decrease in the amount of CaO by ~ 70%. Although our isocon is estimated, a best fit, the data of Figure 10 demonstrate conclusively that serpentinization at Low Divide could not have been isochemical, because the points for each element fall nowhere near a single line through the origin. Only if our estimated bulk composition (harzburgite H3) is very distant from the real protolith (i.e., FeO is off by a quarter of

the amount present) could the serpentinization be nearly isochemical.

The inferred extraction of calcium during serpentinization is consistent with the results of our geochemical models, because no Ca-bearing phase precipitates at high water-to-rock ratios (above 630; note that the rock in the water-to-rock ratios of the models represents the amount of fully dissolved rock; Fig. 8). At a water-to-rock ratio of about 370, about 30 mol% of Ca are precipitated while 70 mol% remain in solution. Removal of CaO is common during serpentinization, as indicated by the strong Ca-enrichment of fluids emanating from serpentinite-hosted hydrothermal systems on the seafloor and on land (e.g., Barnes and O'Neil, 1969; Kelley et al., 2001), as well as the frequent occurrence of local Ca-metasomatism (i.e., rodingitization) associated with serpentinization (e.g., Honnorez and Kirst, 1975). Rodingitization is rare in the Josephine peridotite (Harper, 1984), but small amounts of calcite and aragonite have been reported along fractures in the serpentinites from the Alta Mine (Dunning and Cooper, 1995), and rodingites are known with a few miles of Low Divide. Figure 10 suggests that FeO and SiO_2 were added to the system. While addition of FeO is difficult to explain under current models of serpentinization, addition of SiO_2 (although relatively small in our Isocon model) is consistent with the model that the MSrp formed by addition of a fluid bringing silica to the original harzburgite (see section 5.2).

Reaction pathways during serpentinization

Here, results of petrographic observations, thermodynamic modeling, and mass balance calculations are used to constrain the reactions for global serpentinization of the studied sample. We investigated two hydration reactions, (R6) and (R7), which could account for serpentinization at Low Divide. Reaction (R6) models serpentinization as suggested by mass balance calculations, which invoke addition of ~ 2% SiO_2 and ~ 25% FeO to the original harzburgite during hydration; reaction (R7) models isochemical serpentinization. The serpentinization reactions were constructed in the Mg-Fe-Si-O-H system, constrained by petrography so that hydration of olivine and orthopyroxene to produce serpentine and magnetite directly; i.e., not invoking steps such as formation of brucite with the SSrp. We started with a harzburgite of 70 vol% Fo_{90} olivine and 30 vol% En_{91} orthopyroxene (i.e., harzburgite H3, Table 2). Serpentinite at Low Divide contains both SSrp and MSrp, and considering that both serpentine types have similar compositions (Table 1), the final serpentinite was constrained to contain ~ 78 vol% serpentine with Mg# = 95.

Reaction (R6) is

$$\begin{aligned}19.00(Mg_{0.9}Fe_{0.1})_2SiO_4 + 11.00(Mg_{0.91}Fe_{0.09})SiO_3 \\ + 1.02SiO_{2(aq)} + 1.63FeO_{(aq)} + 32.39H_2O \\ = 15.51(Mg_{0.95}Fe_{0.05})_3Si_2O_5(OH)_4 \\ + 1.36Fe_3O_4 + 1.36H_2 \qquad \text{(R6)},\end{aligned}$$

and reaction (R7) is

$$\begin{aligned}19.00(Mg_{0.9}Fe_{0.1})_2SiO_4 + 11.00(Mg_{0.91}Fe_{0.09})SiO_3 \\ + 30.85H_2O \\ = 15.00(Mg_{0.95}Fe_{0.05})_3Si_2O_5(OH)_4 + 0.85Fe_3O_4 \\ + 1.46MgO + 0.85H_2 \qquad \text{(R7)}.\end{aligned}$$

These reactions are sufficient to successfully model the mineral proportions of the Low Divide serpentinite. Carrying reaction (R6), with FeO and SiO_2 added by the fluid phase, to 74% completion would produce 78.1 vol% serpentine and 2.8 vol% magnetite, with 13.4 vol% and 5.7 vol% relic olivine and orthopyroxene, respectively. Reaction (R6) also allows for addition of 2.5% SiO_2 and 25% FeO to the original harzburgite. Reaction (R7) carried to 73% completion produces 77.6 vol% serpentine and 1.8 vol% magnetite, and leaves behind 14.5 vol% and 6.1 vol% relic olivine and orthopyroxene, respectively. The mineral proportions predicted by reactions (R6) and (R7) differ from those of the real rock by a slight overabundance of orthopyroxene (1-2 vol%). In addition, reaction (R6) involves addition of 2.7% MgO to the original harzburgite. However, the reader should keep in mind that these proportions do have significant uncertainties (that are difficult to quantify), stemming from uncertainties in the compositions of the serpentinite, the inferred protolith, and the compositions and proportions of minerals.

Hydrogen production during serpentinization

Oxidation of the ferrous iron contained in primary minerals to form magnetite is coupled to the production of hydrogen, which can be a source of electrons and chemical energy for a number of biochemical processes (e.g., McCollom, 2007). Fluids venting from serpentinite-hosted hydrothermal systems on the seafloor are characterized by abundant H_2 concentrations (up to 16 mmol/kg of fluid; Kelley et al., 2001; Charlou et al., 2002), consistent with the production of hydrogen during serpentinization. Such systems may host dense microbial communities, whose presence has been shown to be intimately linked to the production of hydrogen during serpentinization (e.g., Kelley et al., 2005). Hydrogen production in ophiolites has

drawn considerable interest (e.g., Schulte et al., 2006; Blank et al., 2009), because the similarity of Mars' crust to terrestrial ocean lithosphere suggests that ophiolites may be good analogs to some Martian environments where life might have existed and may persist today (e.g., Schulte et al., 2006; Blank et al., 2009; Sleep et al., 2011). Schulte et al. (2006) estimated the amount of hydrogen that could be produced during serpentinization of the ultramafic rocks from the Coast Range ophiolite to be at most ~ 500 mol H_2 per m^3 of peridotite. Reaction (R6), when carried to 74% completion, would involve alteration of ~ 14 moles of Fo_{90} olivine (2.07 kg) + ~ 8 moles of En_{91} orthopyroxene (0.84 kg) and would produce ~ 1 mole of H_2. Reaction (R7), carried to 73% completion, would involve alteration of ~ 14 moles of Fo_{90} olivine (2.04 kg) + ~ 8 moles of En_{91} orthopyroxene (0.83 kg) and would produce ~ 0.6 mole of H_2. Assuming molar volumes of 43.5 cm^3/mol for Fo_{90} and 31.6 cm^3/mol for En_{91}, this corresponds to ~ 720–1160 mol H_2/m^3 of rock, broadly consistent with estimates by Schulte et al. (2006). At water-to-rock ratio of 1, this corresponds to ~ 220–350 mmol H_2/kg of fluid. This is 10–20 times higher than the highest H_2 concentrations measured in vent fluids from seafloor serpentinite- hosted hydrothermal systems (e.g., Kelley et al., 2001; Charlou et al., 2002). On the other hand, the abundances of CaO in the original and serpentinized peridotites suggest a higher water-to-rock ratio closer to 370 (see section 5.4). We acknowledge that the use of a single element in a complex, multi-process rock is a simplification, but CaO appears to provide a believable constraint on the reaction progress and the water-to-rock ratio, because much of it has been lost in solution. Assuming a water-to-rock ratio of 370, reactions (R6) and (R7) carried to 74% and 73% completion, respectively, imply production of ~ 0.6–0.9 mmol H_2/kg of fluid, consistent with the molality of H_2(aq) in the thermochemical model at the same water-to-rock ratio (0.9 mmol/kg of fluid). These concentrations are in the lower end of those measured in typical deep-sea vent fluids from serpentinite-hosted hydrothermal systems (Kelley et al., 2001; Note that the values Kelley et al. report in the text are different from the values in the table, we quote the table; Proskurowski et al., 2008).

CONCLUSIONS

We have studied a partially serpentinized peridotite from the Josephine ophiolite using high-spatial resolution petrologic analysis, thermochemical and mineral mass balance models, and element mobility analysis in order to characterize the chemical nature of its serpentinization. Results indicate that brucite never formed as part of the first generation of serpentinization products. Preferential dissolution of orthopyroxene and/or infiltration of a silica-rich fluid under open-system conditions produced serpentine and magnetite as products of the first generation of serpentinization. A second phase of serpentinization might have formed a brucite-bearing assemblage, although brucite is not observed currently; it is likely that original brucite was dissolved or reacted out, leaving that serpentinite (Ssrp) with significant porosity. Alternatively, porosity in late serpentine veins may result from volume expansion of the peridotite during serpentinization. Results were used to constrain the reactions for global serpentinization of the studied sample. These reactions suggest that significant amounts of dissolved H_2 have been produced during the serpentinization of the Josephine peridotite, which could then have been a potential energy source for significant biomass. We acknowledge that using petrography of any serpentinite to estimate dihydrogen production is extremely difficult, and results presented here should be regarded only as general indication. Our study underscores the relevance of a detailed examination of the rocks themselves for improving our understanding of serpentinization and its consequence on geochemical and biochemical systems.

ACKNOWLEGMENTS

All data used to generate this paper are available from the authors upon request. This work was supported by the NASA Astrobiology Institute (NAI), Ames Research Center node [NNX09AN30A], and The Lunar and Planetary Institute. The authors thank Tori Hoeler (NASA-JSC) and Gregory D. Harper for help in collecting the samples. We are also grateful to Anne Peslier (NASA-JSC) for assistance with electron microprobe analyses, and Daniel K. Ross (NASA-JSC) for assistance with scanning electron microscopy. SPS acknowledges an Open University Research Investment Fellowship and support of the LPI though a visiting status. Thoughtful and helpful reviews by two anonymous reviewers and the Associate Editor M. Satish-Kumar are greatly appreciated. LPI Contribution # 2002.

SUPPLEMENTARY MATERIALS

Color version of Figures 1, 3, 7, 8, and 9 is available online from http://doi.org/10.2465/jmps.160509

REFERENCES

Andreani, M., Baronnet, A., Boullier, A.-M. and Gratier, J.P. (2004) A microstructural study of a 'crack-seal' type serpentine vein using SEM and TEM techniques. European Journal

of Mineralogy, 16, 585-595.

Andreani, M., Mevel, C., Boullier, A.-M. and Escartin, J. (2007) Dynamic control on serpentine crystallization in veins: Constraints on hydration processes in oceanic peridotites. Geochemistry, Geophysics, Geosystems, 8, Q02012, doi:10.1029/2006GC001373.

Augustin, N., Lackschewitz, K.S., Kuhn, T. and Devey, C.W. (2008) Mineralogical and chemical mass changes in mafic and ultramafic rocks from the Logatchev hydrothermal field (MAR 15°N). Marine Geology, 256, 18-29.

Aumento, F. and Loubat, H. (1971) The Mid-Atlantic ridge near 45°N. XVI. Serpentinized ultramafic intrusions. Canadian Journal of Earth Sciences, 8, 631-663.

Auzende, A.-L., Devouard, B., Guillot, S., Daniel, I., Baronnet, A. and Lardeaux, J.M. (2002) Serpentinites from central Cuba: Petrology and HRTEM study. European Journal of Mineralogy, 14, 905-914.

Bach, W., Garrido, C.J., Paulick, H., Harvey, J. and Rosner, M. (2004) Seawater-peridotite interactions: first insights from ODP Leg 209, MAR 15°N. Geochemistry, Geophysics, Geosystems, 5, Q09F26, doi:10.1029/2004GC00074.

Bach, W., Paulick, H., Garrido, C.J., Ildefonse, B., Meurer, W.P. and Humphris, S.E. (2006) Unraveling the sequence of serpentinization reactions: petrography, mineral chemistry, and petrophysics of serpentinites from MAR 15°N (ODP Leg 209, Site 1274), Geophysical Research Letters, 33, L13306, doi:10.1029/2006GL025681.

Barnes, I., LaMarche, V.C.Jr. and Himmelberg, G. (1967) Geochemical evidence of present-day serpentinization. Science, 156, 830-832.

Barnes, I. and O'Neil, J.R. (1969) The relationship between fluids in some fresh Alpine-type ultramafics and possible modern serpentinization, Western United States. Geological Society of America Bulletin, 80, 1947-1960.

Barnes, I., Rapp, J.B., O'Neil, J.R., Sheppard, R.A. and Gude, A.J. (1972) Metamorphic assemblages and the direction of flow of metamorphic fluids in four instances of serpentinization. Contribution to Mineralogy and Petrology, 35, 263-276.

Beard, J.S., Frost, B.R., Fryer, P., McCaig, A., Searle, R., Ildefonse, B., Zinin, P. and Sharma, S.K. (2009) Onset and progression of serpentinization and magnetite formation in olivine-rich troctolite from IODP hole U1309D. Journal of Petrology, 50, 387-403.

Blank, J.G., Green, S.J., Blake, D., Valley, J.W., Kita, N.T., Treiman, A. and Dobson, P.F. (2009) An alkaline spring system within the Del Puerto ophiolite (California, USA): a Mars analog site. Planetary and Space Science, 57, 533-540.

Bridges, J.C. and Schwenzer, S.P. (2012) The nakhlite hydrothermal brine on Mars. Earth and Planetary Science Letters, 359, 117-123.

Bridges, J.C., Schwenzer, S.P., Leveille, R., Westall, F., Wiens, R., Mangold, N., Bristow, T., Edwards, P. and Berger, G. (2015) Diagenesis and clay formation at Gale Crater, Mars. Journal of Geophysical Research, 120, doi:10.1002/2014JE004757.

Burkhard, D.J.M. (1993) Accessory chromium spinels: Their coexistence and alteration in serpentinites. Geochimica et Cosmochimica Acta, 57, 1297-1306.

Cannat, M. (1993) Emplacement of mantle rocks in the seafloor at mid-ocean ridges. Journal of Geophysical Research, 98, 4163-4172.

Cannat, M., Bideau, D. and Bougault, H. (1992) Serpentinized peridotites and gabbros in the Mid-Atlantic Ridge axial valley at 15°37′N and 16°52′N. Earth and Planetary Science Letters, 109, 87-106.

Charlou, J.L., Donval, J.P., Fouquet, Y., Jean-Baptiste, P. and Holm, N.G. (2002) Geochemistry of high H_2 and CH_4 vent fluids issuing from ultramafic rocks at the Rainbow hydrothermal field (36°14′N, MAR). Chemical Geology, 191, 345-359.

Coleman, R.G. (1971) Petrologic and geophysical nature of serpentinites. Geological Society of America Bulletin, 82, 897-918.

Coleman, R.G. and Keith, T.E. (1971) A chemical study of serpentinization-Burro Mountain, California. Journal of Petrology, 12, 311-328.

Coulton, A.J., Harper, G.D. and O'Hanley, D.S. (1995) Oceanic versus emplacement age serpentinization in the Josephine ophiolite: implications for the nature of the Moho at intermediate and slow spreading ridges. Journal of Geophysical Research, 100, 22245-22260.

Da Costa, I.R., Barriga, F.J., Viti, C., Mellini, M. and Wicks, F.J. (2008) Antigorite in deformed serpentinites from the Mid-Atlantic Ridge. European Journal of Mineralogy, 20, 563-572.

Dawson, P., Hadfield, C.D. and Wilkinson, G.R. (1973) The polarized infra-red and Raman spectra of $Mg(OH)_2$ and $Ca(OH)_2$. Journal of Physics and Chemistry of Solids, 34, 1217-1225.

Dick, H.J.B. (1974) Terrestrial nickel-iron from the Josephine peridotite, its geological occurrence, associations, and origin. Earth and Planetary Science Letters, 24, 291-298.

Dick, H.J.B. (1977) Partial melting in the Josephine peridotite-I. The effect on mineral composition and its consequences for geobarometry and geothermometry. American Journal of Science, 277, 801-832.

Dunning, G.E. and Cooper, Jr.J.F. (1995) Troilite from the Low Divide District, Del Norte County, California. California Geology, 48, 119-128.

Escartín, J. and Cannat, M. (1999) Ultramafic exposures and the gravity signature of the lithosphere near the Fifteen-Twenty Fracture Zone (Mid-Atlantic Ridge, 14°-16.5°N). Earth and Planetary Science Letters, 171, 411-424.

Escartín, J., Hirth, G. and Evans, B. (2001) Strenght of slightly serpentinized peridotites: implications for the tectonics of oceanic lithosphere. Geology, 29, 1023-1026.

Evans, K.A., Powell, R. and Frost, B.R. (2013) Using equilibrium thermodynamics in the study of metasomatic alteration, illustrated by an application to serpentinites. Lithos, 168, 67-84.

Filiberto, J. and Schwenzer, S.P. (2013) Alteration mineralogy of the Home Plate and Columbia Hills - formation conditions in context to impact, volcanism, and fluvial activity. Meteoritics and Planetary Science, 48, 1937-1957.

Frost, B.R. and Beard, J.S. (2007) On silica activity and serpentinization. Journal of Petrology, 48, 1351-1368.

Frost, B.R., Evans, K.A., Swapp, S.M., Beard, J.S. and Mothersole, F.E. (2013) The process of serpentinization in dunite from New Caledonia. Lithos, 178, 24-39.

Gràcia, E., Charlou, J.-L., Radford-Knoery, J. and Parson, L.M. (2000) Non-transform offsets along the Mid-Atlantic Ridge south of the Azores (38°N-34°N): ultramafic exposures and hosting of hydrothermal vents. Earth and Planetary Science Letters 177, 89-103.

Grant, J.A. (1986) The isocon diagram-A simple solution to Gresen's equation for metasomatic alteration. Economic Geology, 81, 1976-1982.

Grant, J.A. (2005) Isocon analysis: A brief review of the method and applications. Physics and Chemistry of the Earth, 30, 997-1004.

Groppo, C., Rinaudo, C., Cairo, S., Gastaldi, D. and Compagnoni, R. (2006) Micro-Raman spectroscopy for a quick and reliable identification of serpentine minerals form ultramafics. European Journal of Mineralogy, 18, 319-329.

Harper, G.D. (1980) The Josephine ophiolite-Remains of a Late Jurassic marginal basin in northern California. Geology, 8, 333-337.

Harper, G.D. (1984) The Josephine ophiolite, northwestern California. Geological Society of America Bulletin, 95, 1009-1026.

Harper, G.D. and Wright, J.E. (1984) Middle to Late Jurassic tectonic evolution of the Klamath Mountains, California-Oregon. Tectonics, 3, 759-772.

Himmelberg, G.R. and Loney, R.A. (1973) Petrology of the Vulcan Peak alpine-type peridotite, southwestern Oregon. Geological Society of America Bulletin, 84, 1585-1600.

Honnorez, J. and Kirst, P. (1975) Petrology of rodingites from the equatorial Mid-Atlantic fracture zones and their geotectonic significance. Contributions to Mineralogy and Petrology, 49, 233-257.

Hostetler, P.B., Coleman, R.G., Mumpton, F.A. and Evans, B.W. (1966) Brucite in Alpine Serpentinites. American Mineralogist, 51, 75-98.

Irwin, W.P. (1972) Terranes of the western Paleozoic and Triassic belt in the Southern Klamath Mountains, California. U.S. Geological Survey Professional Paper, 800-C, 103-111.

Janecky, D.R. and Seyfried, Jr.W.E. (1986) Hydrothermal serpentinization of peridotite within the oceanic crust: Experimental investigations of mineralogy and major element chemistry. Geochimica et Cosmochimica Acta, 50, 1357-1378.

Jöns, N., Bach, W. and Klein, F. (2010) Magmatic influence on reaction paths and element transport during serpentinization. Chemical Geology, 274, 196-211.

Jordan, G. and Rammensee, W. (1996) Dissolution rates and activation energy for dissolution of brucite (001): A new method based on the microtopography of crystal surfaces. Geochimica et Cosmochimica Acta, 60, 5055-5062.

Katayama, I., Kurosaki, I. and Hirauchi, K.I. (2010) Low silica activity for hydrogen generation during serpentinization: An example of natural serpentinites in the Mineoka ophiolite complex, central Japan. Earth and Planetary Science Letters, 298, 199-204.

Kelley, D.S., Karson, J.A., Blackman, D.K., Früh-Green, G.L., Butterfield, D.A., Lilley, M.D., Olson, E.J., Schrenk, M.O., Roe, K.K., Lebon, G.T. and Rivizzigno, P. (2001) An off-axis hydrothermal vent field near the Mid-Atlantic Ridge at 30°N. Nature, 412, 145-149.

Kelley, D.S., Karson, J.A., Früh-Green, G.L., Yoerger, D.R., Shank, T.M., Butterfield, D.A., Hayes, J.M., Schrenk, M.O., Olson, E.J., Proskurowski, G., Jakuba, M., Bradley, A., Larson, B., Ludwig, K., Glickson, D., Buckman, K., Bradley, A.S., Brazelton, W.J., Roe, K., Elend, M.J., Delacour, A., Bernasconi, S.M., Lilley, M.D., Baross, J.A., Summons, R.E. and Sylva, S.P. (2005) A serpentinite-hosted ecosystem: the Lost City hydrothermal field. Science, 307, 1428-1434.

Kimball, K.L. (1990) Effects of hydrothermal alteration on the compositions of chromian spinels. Contributions to Mineralogy and Petrology, 105, 337-346.

Klein, F., Grozevaz, N.G., Seewald, J.S., McCollom, T.M., Humphris, S.E., Moskowitz, B., Berquó, T.S. and Kahl, W.-A. (2015) Experimental contraints on fluid-rock reactions during incipient serpentinization of harzburgite. American Mineralogist, 100, 991-1002.

Lafay, R., Deschamps, F., Schwartz, S., Guillot, S., Godard, M., Debret, B. and Nicollet, C. (2013) High-pressure serpentinites, a trap-and-release system controlled by metamorphic conditions: Example from the Piedmont zone of the western Alps. Chemical Geology, 343, 38-54.

Lin, F.C. and Clemency, C.V. (1981) The dissolution kinetics of brucite, antigorite, talc, and phlogopite at room temperature and pressure. American Mineralogist, 66, 801-806.

Loney, R.A. and Himmelberg, G.R. (1976) Structure of the Vulcan Peak alpine-type peridotite, southwestern Oregon. Geological Society of America Bulletin, 87, 259-274.

McCollom, T.M. (2007) Geochemical constraints on sources of metabolic energy for chemolithoautotrophy in ultramafic-hosted deep-sea hydrothermal systems. Astrobiology, 7, 933-950.

Melwani Daswani, M., Schwenzer, S.P., Reed, M.H., Wright, I.P. and Grady, M.M. (2016) Fluids on early Mars: new insights from an old meteorite. Meteoritics and Planetary Science, 51, 2154-2174.

Mével, C. (2003) Serpentinization of abyssal peridotites at mid-ocean ridges. Comptes Rendus Geoscience, 335, 825-852.

Miller, D.J. and Christensen, N.I. (1997) Seismic velocities of lower crustal and upper mantle rocks from the slow-spreading Mid-Atlantic Ridge, South of the Kane transform zone (MARK area). Proceedings of the Ocean Drilling Program. Scientific Results (Karson, J.A., Cannat, M., Miller, D.J. and Elthon, D. Eds.). 153. Ocean Drilling Program, College Station, Texas, 437-454.

Miyashiro, A., Shido, F. and Ewing, M. (1969) Composition and origin of serpentinites from the Mid-Atlantic Ridge near 24° and 30° North latitude. Contributions to Mineralogy and Petrology, 23, 117-127.

Nakamura, K., Morishita, T., Bach, W., Klein, F., Hara, K., Okino, K., Takai, K. and Kumagai, H. (2009) Serpentinized troctolites exposed near the Kairei Hydrothermal Field, Central Indian Ridge: Insights into the origin of the Kairei hydrothermal fluid supporting a unique microbial ecosystem. Earth and Planetary Science Letters, 280, 128-136.

Norrell, G.T., Teixell, A. and Harper, G.D. (1989) Microstructure of serpentinite mylonites from the Josephine ophiolite and serpentinization in retrogressive shear zones, California. Geological Society of America Bulletin, 101, 673-682.

O'Hanley, D.S. (1992) Solution to the volume problem in serpentinization. Geology, 20, 705-708.

O'Hanley, D.S. and Offler, R. (1992) Characterization of multiple serpentinization, Woodsreef, New South Wales. Canadian Mineralogist, 30, 1113-1126.

Okland, I., Huang, S., Dahle, H., Thorseth, I.H. and Pedersen, R.B. (2012) Low temperature alteration of serpentinized ultramafic rock and implications for microbial life. Chemical Geology, 318, 75-87.

Oufi, O., Cannat, M. and Horen, H. (2002) Magnetic properties of variably serpentinized abyssal peridotites. Journal of Geophysical Research: Solid Earth, 107, doi:10.1029/2001JB000549.

Page, N.J. (1976) Serpentinization and alteration in an olivine cumulate from the Stillwater Complex, southwestern Montana. Contribution to mineralogy and Petrology, 54, 127-137.

Pokrovsky, O.S. and Schott, J. (2004) Experimental study of brucite dissolution and precipitation in aqueous solutions: surface speciation and chemical affinity control. Geochimica et Cosmochimica Acta, 68, 31-45.

Proskurowski, G., Lilley, M.D., Seewald, J.S., Früh-Green, G.L., Olson, E.J., Lupton, J.E., Sylva, S.P. and Kelley, D.S. (2008) Abiogenic hydrocarbon production at Lost City hydrothermal field. Science, 319, 604-607.

Ramana, Y.V., Gogte, B.S. and Sarma, K.V.L.N.S. (1981) Study of preferred orientation in fine grained rocks (serpentinites from the indus ophiolitic belt, Kashmir Himalaya, India) by an acoustic method. Geoexploration, 19, 81-89.

Reed, M.H. (1982) Calculation of multicomponent chemical equilibria and reaction processes in systems involving minerals, gases and an aqueous phase. Geochimica et Cosmochimica Acta, 46, 513-528.

Reed, M.H. (1983) Seawater-basalt reaction and the origin of greenstones and related ore deposits. Economic Geology, 78, 466-485.

Reed, M.H. (1998) Calculation of simultaneous chemical equilibria in aqueous-mineral-gas systems and its application to modeling hydrothermal processes. In Techniques in hydrothermal ore deposits geology (Richards, J.P. and Larson, P.B. Eds.). pp. 252, Reviews in Economic Geology, 10, Society of Economic Geologists, Littleton, Colorado, 109-124.

Reed, M.H. and Spycher, N.F. (2006) User guide for CHILLER: A program for computing water-rock reactions, boiling, mixing, and other reaction processes in aqueous-mineral-gas systems and Minplot guide (3rd Ed.). pp. 76, University of Oregon, Eugene, Oregon.

Reed, M.H., Spycher, N.F. and Palandri, J. (2010) User guide for CHIM-XPT: A program for computing reaction processes in aqueous-mineral-gas systems and Minplot guide. pp. 73, University of Oregon, Eugene, Oregon.

Rinaudo, C., Gastaldi, D. and Belluso, E. (2003) Characterization of chrysotile, antigorite, and lizardite by FT-Raman spectroscopy. The Canadian Mineralogist, 41, 883-890.

Russell, M.J., Hall, A.J. and Martin, W. (2010) Serpentinization as a source of energy at the origin of life. Geobiology, 8, 355-371.

Saleeby, J., Harper, G.D., Snoke, A.W. and Sharp, W. (1982) Time relations and structural-stratigraphic patterns in ophiolite accretion, west-central Klamath Mountains, California. Journal of Geophysical Research, 87, 3831-3848.

Schulte, M., Blake, D., Hoehler, T. and McCollom, T. (2006) Serpentinization and its implications for life on the early Earth and Mars. Astrobiology, 6, 364-376.

Schwenzer, S.P. and Kring, D.A. (2009) Impact-generated hydrothermal systems: capable of forming phyllosilicates on Noachian Mars. Geology, 37, 1091-1094.

Schwenzer, S.P., Abramov, O., Allen, C.C., Clifford, S., Cockell, C.S., Filiberto, J., Kring, D.A., Lasue, J., McGovern, P.J., Newsom, H.E., Treiman, A.H., Vaniman, D.T. and Wiens, R.C. (2012) Puncturing Mars: How impact craters interact with the Martian cryosphere. Earth and Planetary Science Letters, 335, 9-17.

Schwenzer, S.P. and Kring, D.A. (2013) Alteration minerals in impact-generated hydrothermal systems - exploring host rock variability. Icarus, 226, 487-496.

Schwenzer, S.P., Bridges, J.C., Wiens, R.C., Conrad, P.G., Kelley, S.P., Leveille, R., Mangold, N., Martìn-Torres, J., McAdam, A., Newson, H., Zorzano, M.P., Rapin, W., Sray, J., Treiman, A.H., Westall, F., Fairèn, A.G. and Meslin, Y.-P. (2016) Fluids during diagenesis and sulfate vein formation in sediments at Gale Crater, Mars. Meteoritics and Planetary Science, 51, 2175-2202.

Shervais, J.W., Kolesar, P. and Andreasen, K. (2005) A field and chemical study of serpentinization - Stonyford, California: chemical flux and mass balance. International Geology Review, 47, 1-23.

Sleep, N.H., Bird, D.K. and Pope, E.C. (2011) Serpentinite and the dawn of life. Philosophical Transactions of the Royal Society B: Biological Sciences, 366, 2857-2869.

Snow, J.E. and Dick, H.J.B. (1995) Pervasive magnesium loss by marine weathering of peridotite. Geochimica and Cosmochimica Acta, 59, 4219-4235.

Spycher, N.F. and Reed, M.H. (1988) Fugacity coefficients of H_2, CO_2, CH_4, H_2O and of H_2O- CO_2-CH_4 mixtures: A virial equation treatment for moderate pressures and temperatures applicable to calculations of hydrothermal boiling. Geochimica and Cosmochimica Acta, 52, 739-749.

Takai, K., Gamo, T., Tsunogai, U., Nakayama, H., Nealson, K.H. and Horikoshi, K. (2004) Geochemical and microbiological evidence for a hydrogen-based, hyperthermophilic subsurface lithoautotrophic microbial ecosystem (HyperSLiME) beneath an active deep-sea hydrothermal field. Extremophiles, 8, 269-282.

Toft, P.B., Arkani-Hamed, J. and Haggerty, S.E. (1990) The effects of serpentinization on density and magnetic susceptibility; a petrophysical model. Physics of the Earth and Planetary Interiors, 65, 137-157.

Wright, J.E. and Wyld, S.J. (1986) Significance of xenocrystic Precambrian zircon contained within the southern continuation of the Josephine ophiolite: Devils Elbow ophiolite remnant, Klamath Mountains, northern California. Geology, 14, 671-674.

Manuscript received May 9, 2016
Manuscript accepted February 1, 2017

Manuscript handled by M. Satish-Kumar